Scaling and parametrization of clear-sky solar radiation over complex topography

Scaling and parametrization of clear-sky solar radiation over complex topography

Richard Essery[1] and Danny Marks[2]

Received 14 June 2006; revised 23 January 2007; accepted 28 January 2007; published 26 May 2007.

[1] Solar radiation at the land surface is influenced by slope, aspect, shadows, and obstruction of the sky, all of which vary over a wide range of length scales in regions of complex topography, with important consequences for the surface energy balance. Atmospheric models, however, generally assume the surface to be flat on subgrid scales. For four areas in North America, ranging in latitude from 39N to 69N and in topography from rolling to mountainous, we simulate spatial patterns of clear-sky incoming solar radiation. It is found that distributions of slope components and variations in shaded area with solar elevation can be approximated by simple functions that scale to each of the areas studied. From these results, parametrizations are developed for averages, standard deviations, and distributions of direct-beam and diffuse solar radiation. Results from these parametrizations, and from a modified form of a simpler parametrization presented previously, compare well with statistics from the spatial simulations. The only topographic input required by the parametrizations is the standard deviation of slope components; this parameter is again found to have simple scaling relationships with the resolution and extent of the underlying elevation grid and with the standard deviation of elevation.

Citation: Essery, R., and D. Marks (2007), Scaling and parametrization of clear-sky solar radiation over complex topography, *J. Geophys. Res.*, *112*, D10122, doi:10.1029/2006JD007650.

1. Introduction

[2] Land surface models are used in atmospheric models to calculate fluxes of heat and moisture as lower boundary conditions for differential equations representing the dynamics and thermodynamics of the atmosphere. Surface state variables such as snow cover and soil moisture are also modelled, and land surface models are increasingly being used to calculate carbon fluxes and storage in coupled climate and carbon cycle models [*Cox et al.*, 2000]. The properties of the land surface and the meteorology of the lower levels of the atmosphere are invariably heterogeneous on the scales of the grids on which these models are applied—kilometers for mesoscale atmospheric models to hundreds of kilometers for global climate models. Several approaches have been adopted for dealing with landscape and meteorological heterogeneity. Distributed models with high-resolution grids (tens of meters) have been used extensively to model processes such as snowmelt [*Kirnbauer et al.*, 1994; *Marks et al.*, 1999], but they are prohibitively expensive for application over large areas. Models using effective parameters describing subgrid surfaces as a whole are much more economical, but due to nonlinearity in the processes involved, there are unlikely to be simple relationships between local and effective parameters [*Shuttleworth*, 1988]. Land surface heterogeneity has been represented by gathering distinct surface types within grid cells into homogeneous tiles for which calculations are performed separately [*Avissar and Pielke*, 1989; *Koster and Suarez*, 1992; *Essery et al.*, 2003], and an analogous approach has been used to account for variations in air temperature and precipitation due to subgrid orography by dividing grid cells into fixed elevation bands [*Arola and Lettenmaier*, 1996; *Essery*, 2003] or using a dynamic snowline [*Walland and Simmonds*, 1996; *Sloan et al.*, 2004]. The Météo France Safran-Crocus-Mepra system [*Durand et al.*, 1999] divides massifs into elevation and aspect bands to model snowpack conditions for avalanche forecasting, but this level of sophistication is unfeasible for large-scale models. *Avissar* [1992] suggested a statistical-dynamical approach to representing surface heterogeneity by integrating the energy balance over probability density functions for surface parameters and illustrated this by coupling a one-dimensional atmospheric model to a land surface model with a distribution of stomatal conductances. Probabilistic approaches have been more commonly used in hydrological models to represent subgrid variations in surface characteristics such as infiltration capacity [*Wood et al.*, 1992]. For meteorological variables, rainfall distributions are often used in models of infiltration and runoff [*Shuttleworth*, 1988], and *Bowling et al.* [2004] used a parametrization of windflow distributions over topography developed by *Essery* [2001] in a model of snow redistribution. An analogous approach might be used to parametrize the

[1]Centre for Glaciology, Institute of Geography and Earth Sciences, University of Wales Aberystwyth, Aberystwyth, UK.
[2]USDA Agricultural Research Service, Northwest Watershed Research Center, Boise, Idaho, USA.

0148-0227/07/2006JD007650

influences of spatial variations in meteorology on the surface energy balance.

[3] Solar radiation incident on the land surface under clear skies varies strongly with slope and aspect and on whether or not the surface lies in the shadow of remote topography; the relative importance of these factors in generating spatial variability in surface radiation has been investigated by *Oliphant et al.* [2003]. Solar radiation variations have strong influences on surface energy balances and have been the subject of long-standing interest [*Kondratyev and Manolova*, 1960; *Garnier and Ohmura*, 1968], but it was only with the availability of gridded elevation data sets, powerful computers, and efficient algorithms [*Dozier and Frew*, 1990] that simulations over large grids became possible. Simulations of variations in solar radiation over topography have been used in predicting things as diverse as snowmelt [*Blöschl et al.*, 1991; *Marks et al.*, 1999; *Lundquist and Flint*, 2006], soil temperatures [*Fu and Rich*, 2002], natural vegetation cover [*Franklin*, 1998], crop yields [*Reuter et al.*, 2005], distribution and energy balance of glaciers [*Arrell and Evans*, 2003; *Strasser et al.*, 2004], likely locations for ice deposits in permanent shadows on the moon [*Margot et al.*, 1999] and the influences of variations in illumination on remote sensing [*Baral and Gupta*, 1997; *Agassi and Ben Yosef*, 1997]. Climate models and numerical weather prediction models have, however, almost exclusively assumed the land surface to be flat on subgrid scales for the purpose of calculating the radiative components in their surface energy budgets although *Hauge and Hole* [2003] investigated the influence of allowing for sloping but plane grid cells in a high-resolution mesoscale model, and *Müller and Scherer* [2005] found that implementing a subgrid radiation parametrization in a mesoscale model gave better temperature forecasts. Radiation correction factors can be calculated explicitly in a preprocessing step and then read from lookup tables by an atmospheric model, giving no computational overhead, but this method requires detailed topographic information. This paper presents an alternative approach using functional parametrizations based on simple topographic statistics.

[4] Parametrizations of the spatial average and standard deviation of direct-beam solar radiation were developed by *Dubayah et al.* [1990] for topography with negligible shading. Statistical characterization of shading in mountainous topography was investigated by *Essery* [2004], and that work is extended here to derive statistical characterizations of solar radiation. Distributions of slope components calculated from digital elevation models (DEMs) are discussed in the next section. Parametrizations are then developed for the average and standard deviation of direct-beam solar radiation, shaded fractions, and sky view factors in section 3; results from the new parametrization and a modified form of the parametrization of *Dubayah et al.* [1990] are compared with gridded simulations of solar radiation for four sites of varying topography. Finally, the scaling of the necessary topographic parameters with the resolution of the DEM is discussed in section 4.

2. Topographic Statistics

[5] Results will be presented for a transect of North American sites with contrasting topography and climate: Trail Valley Creek (69N, 133W) in the Northwest Territories, Wolf Creek (60N, 135W) in the Yukon, Reynolds Creek (43N, 117W) in Idaho, and Maroon Creek (39N, 107W) in Colorado. Extensive hydrological and micrometeorological investigations have been conducted in all of these regions. The Trail Valley Creek and the Wolf Creek Research Basin were the study sites for the Mackenzie GEWEX study (*Rouse*, 1999). The Reynolds Creek Experimental Watershed has been used for hydrological research and monitoring since 1960 [*Slaughter et al.*, 2001]. Maroon Creek lies within the Large Regional Study Area of the NASA Cold Land Processes Experiment (CLPX; *Cline et al.*, 1999) and was selected here as an area of particularly steep and anisotropic topography. Data from Wolf Creek, Reynolds Creek, and CLPX sites in Colorado are also being used in a study of snow processes in North American mountain environments under the GEWEX Americas Prediction Project. Figure 1 shows the contour maps for each site, shaded with the conventional illumination from the northwest; a $12 \times 12\text{-km}^2$ area with elevations specified by a 30-m DEM is shown in each case. Edge effects will be reduced by only calculating topographic and radiation statistics for the central $10 \times 10\text{-km}^2$ areas (comparable in size to the grid cells of a mesoscale model). Average slopes are 2 for Trail Valley Creek, 13 for Wolf Creek and Reynolds Creek, and 27 for Maroon Creek.

[6] In terms of partial derivatives of elevation z with respect to horizontal distances x (increasing toward the east) and y (increasing toward the north), the component of the surface slope along azimuth ϕ is

$$s(\phi) = \cos\phi\frac{\partial z}{\partial y} - \sin\phi\frac{\partial z}{\partial x}, \tag{1}$$

where the solar convention that azimuths are measured as positive anticlockwise from south has been used. The average of s will be close to zero for a large area without a significant overall slope, and equation (1) then gives the variance as

$$\sigma^2(\phi) = \sin^2\phi\overline{\left(\frac{\partial z}{\partial x}\right)^2} + \cos^2\phi\overline{\left(\frac{\partial z}{\partial y}\right)^2} - 2\sin\phi\cos\phi\overline{\frac{\partial z}{\partial x}}\,\overline{\frac{\partial z}{\partial y}}, \tag{2}$$

which, for moderate anisotropy, can be approximated by an ellipse

$$\sigma^2(\phi) = \frac{\sigma_+\sigma_-}{\sigma_+^2 - \left(\sigma_+^2 - \sigma_-^2\right)\cos^2\left(\phi - \phi_+\right)}, \tag{3}$$

where σ_+ is the maximum value of σ, ϕ_+ is the azimuth for which it occurs, and σ_- is the minimum value in the perpendicular direction. Topography that is statistically isotropic gives a constant value of σ for all azimuths; a necessary condition for this to occur is that slope components in perpendicular directions are uncorrelated. Standard deviations of slope components calculated from the DEMs are shown in Figure 2. The standard deviation for Trail Valley Creek is small (0.04) and nearly independent of azimuth. Wolf Creek and Reynolds Creek have similar standard deviations (around 0.2) although Wolf Creek

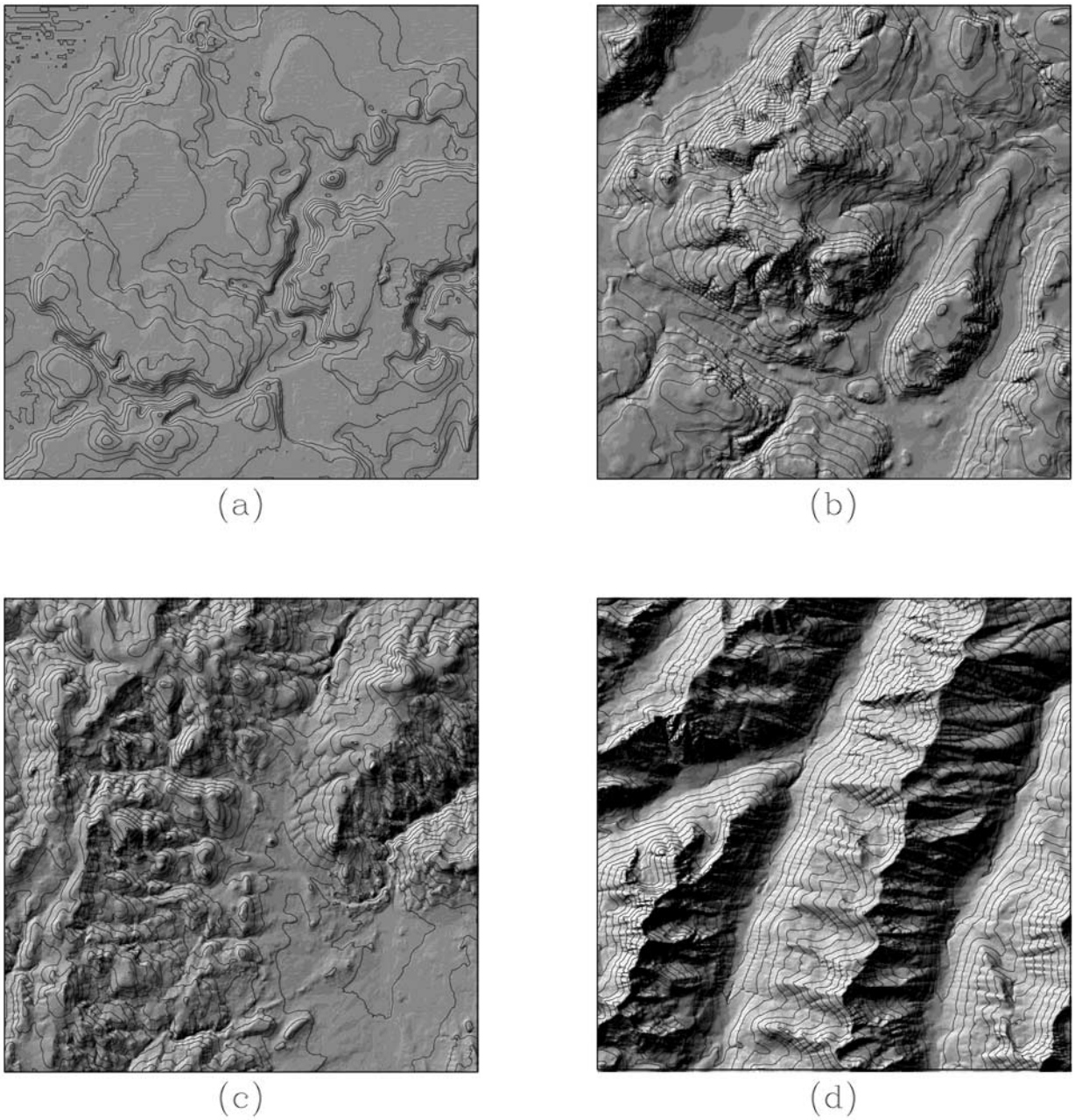

Figure 1. Contour maps shaded with illumination from the northwest at an elevation of 45 for (a) Trail Valley Creek, (b) Wolf Creek, (c) Reynolds Creek, and (d) Maroon Creek. The areas shown are 12 × 12 km^2, and the contour interval is 10 m in Figure 1a, 50 m in Figures 1b and 1c, and 100 m in Figure 1d.

shows more anisotropy. Maroon Creek has the largest standard deviation (averaging 0.4) and a clear anisotropy, with larger standard deviations for slope components across the main ridges; equation (3) fits the azimuth dependence well.

[7] *Essery* [2001] found that distributions of slope components for Trail Valley Creek had broad tails and could be approximated by a Laplace distribution

$$p(s) = \frac{1}{\sqrt{2}\sigma} \exp\left(-\sqrt{2}\frac{|s|}{\sigma}\right) \quad (4)$$

with zero mean and standard deviation σ. The same function was found to give reasonable approximations to slope component distributions for tundra topography in Alaska [*Bowling et al.*, 2004] and mountainous regions in North Wales and the French Alps [*Essery*, 2004]. Figure 3 shows the distributions of southerly slope components, normalized by their standard deviations so that they can be compared with a single Laplace distribution, for each of the sites studied here. The fits are not exact and would be rejected by chi-square tests, but the true test for the use of the Laplace distribution here will be how well it predicts

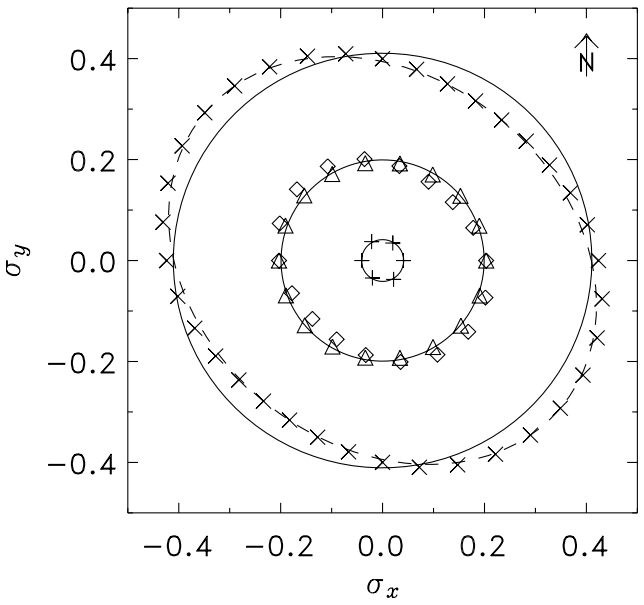

Figure 2. Polar plot of standard deviations of slope components for Trail Valley Creek (+), Wolf Creek (◇), Reynolds Creek (△), and Maroon Creek (×). Solid lines are circles showing average standard deviations, and the dashed line is an ellipse, defined by equation (3), fitted to the statistics for Maroon Creek.

statistics of radiation distributions in comparison with gridded simulations.

3. Statistical Radiation Geometry

[8] Many models for calculating distributions of solar radiation over topographic grids have been developed [e.g., *Garnier and Ohmura*, 1968; *Dozier and Frew*, 1990; *Dubayah and Rich*, 1995; *Kumar et al.*, 1997; *Mckenney et al.*, 1999; *Corripio,* 2003], but all of them implement the same basic geometric principles. The direct-beam solar radiation on a sun-lit point is lS_0, where S_0 is the radiation on a plane perpendicular to the solar rays and the direct-beam illumination fraction l is given by the scalar product between unit vectors normal to the slope and in the direction of the sun, provided that this quantity is positive; slopes for which it is negative are self-shaded and receive no direct-beam radiation. Points that are not self-shaded will still be in shadow if the sun lies below the local horizon, i.e., if the angle from a point to its horizon in the direction of the sun exceeds the solar elevation. Separate calculations determine if a point is either self-shaded or horizon-shaded although, in fact, any point that is self-shaded is also horizon-shaded [*Koenderink et al.*, 1999; *Essery*, 2004]. For solar elevation θ, l is given by

$$l = \frac{\sin\theta + s_\parallel \cos\theta}{\left(1 + s_\perp^2 + s_\parallel^2\right)^{1/2}} \tag{5}$$

for $s_\parallel > -\tan\theta$, and is zero otherwise, where $s_\parallel$ is the surface slope component in the direction of the solar azimuth, and $s_\perp$ is the component in the perpendicular direction; l is more commonly expressed as a function of slope and aspect angles, but it is given here in terms of slope components because of the simple scaling form found above for their distributions.

[9] The fraction of an area that is self-shaded for solar elevation θ is

$$f_{\mathrm{self}} = \int_{-\infty}^{-\tan\theta} p(s)ds, \tag{6}$$

which, with $p(s)$ from equation (4), gives

$$f_{\mathrm{self}} = \frac{1}{2}\exp\left(-\frac{\sqrt{2}}{\sigma}\tan\theta\right). \tag{7}$$

Figure 4a shows self-shaded fractions calculated from the DEMs for varying solar elevations and a southerly azimuth; results plotted against $\sigma^{-1}\tan\theta$ all fall close to a single curve defined by equation (7).

[10] For a point on the surface, the horizon angle η in some direction is the maximum angle to any other point on the surface in that direction [*Dozier and Frew*, 1990], and so, over a large enough area, horizon angles can be expected to have a cumulative probability following the extreme value distribution [*Gumbel*, 1958]

$$P(\eta > \theta) = 1 - \exp\left[-\exp\left(\frac{a-\theta}{b}\right)\right]. \tag{8}$$

The parameters of equation (8) are $b = \sqrt{6}\sigma_\eta/\pi$ and $a = \overline{\eta} - \gamma b$, where $\overline{\eta}$ and σ_η are the average and standard deviation of the horizon angles, and $\gamma \approx 0.5772$ is the Euler's constant. Points at which the horizon angle exceeds the solar elevation are shaded, so the fraction of the surface in shadow is $f_{\mathrm{shad}}(\theta) = P(\eta > \theta)$. Plotting f_{shad} against $(\theta - a)/b$, the simulation results should, again, collapse onto a single curve; this is confirmed by Figure 4b.

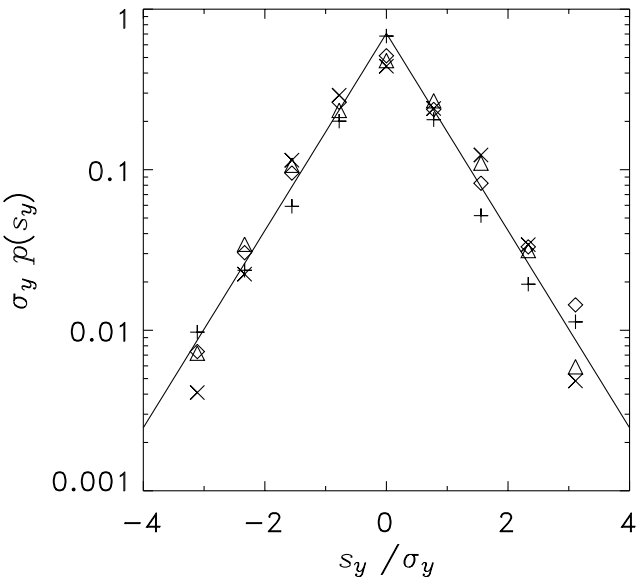

Figure 3. Distributions of normalized southerly slope components (symbols as in Figure 2). The line is a Laplace distribution.

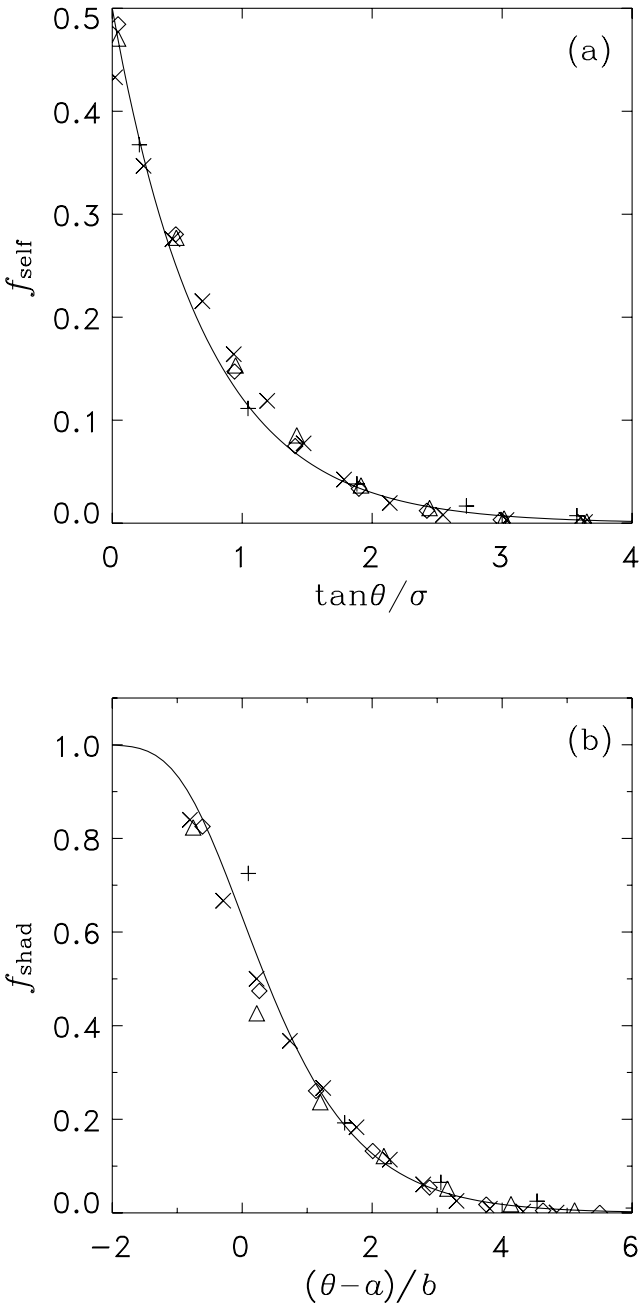

Figure 4. (a) Self-shaded fractions and (b) horizon-shaded fractions against scaled solar elevation (symbols as in Figure 2). The lines are taken from equation (7) in Figure 4a and equation (8) in Figure 4b.

[11] Neglecting horizon shading for the moment, average values of $\bar{l}$ and $\bar{l^2}$ are given by the integrals

$$\bar{l} = \int_{-\tan\theta}^{\infty} ds_{\parallel} \int_{-\infty}^{\infty} ds_{\perp} \frac{\sin\theta + s_{\parallel}\cos\theta}{\left(1 + s_{\perp}^2 + s_{\parallel}^2\right)^{1/2}} p(s_{\parallel}, s_{\perp}) \qquad (9)$$

and

$$\bar{l^2} = \int_{-\tan\theta}^{\infty} ds_{\parallel} \int_{-\infty}^{\infty} ds_{\perp} \frac{(\sin\theta + s_{\parallel}\cos\theta)^2}{1 + s_{\perp}^2 + s_{\parallel}^2} p(s_{\parallel}, s_{\perp}), \qquad (10)$$

from which the standard deviation of l is found as $\sigma_l = (\bar{l^2} - \bar{l}^2)^{1/2}$. Assuming a uniform distribution of slope aspects and constant slope angle, and neglecting self-shading, *Dubayah et al.* [1990] were able to evaluate integrals analogous to equations (9) and (10) analytically to find

$$\bar{l} = \cos\psi \sin\theta \qquad (11)$$

and

$$\sigma_l = 2^{-1/2} \sin\psi \cos\theta \qquad (12)$$

for average slope angle ψ. The standard deviation of slope components along any azimuth for this distribution is $2^{-1/2}$ tan ψ, suggesting alternative formulations

$$\bar{l} = \cos\left(\tan^{-1}\sqrt{2}\sigma\right) \sin\theta \qquad (13)$$

and

$$\sigma_l = 2^{-1/2} \sin\left(\tan^{-1}\sqrt{2}\sigma\right) \cos\theta. \qquad (14)$$

[12] The joint probability $p(s_{\parallel}, s_{\perp})$ separates into the product $p(s_{\parallel})p(s_{\perp})$ for isotropic topography, but the integrals in equations (9) and (10) are intractable for the distribution given by equation (4), so some numerical or approximate techniques are required to evaluate them. Monte-Carlo integrations can be performed by generating two series of random numbers following equation (4) and averaging values of l and l^2 calculated from equation (5) using these series as $s_{\parallel}$ and $s_{\perp}$; correlated or uncorrelated series can be used as necessary. This procedure is useful for investigating the behaviors of the integrals, but the calculations are still expensive, and analytic approximations would be more useful for practical applications. Replacing $s_{\perp}^2 + s_{\parallel}^2$ in the denominators of equations (9) and (10) by the expectation value $2\sigma^2$, the integrals can be approximated by

$$\bar{l} = \frac{\sin\theta + 2^{-1/2}\sigma f_{self}\cos\theta}{(1 + 2\sigma^2)^{1/2}} \qquad (15)$$

and

$$\bar{l^2} = \frac{(1 + 0.2\sigma^3)\sin^2\theta + \sigma^2(1 - f_{self})\cos^2\theta}{1 + 2\sigma^2}. \qquad (16)$$

The σ^3 term in equation (16) is an empirical correction to match the σ dependence found in Monte-Carlo integrations at large solar elevations. These expressions include self-shading but not horizon shading. Assuming random overlap of shadows gives the corrections

$$\bar{l} = \left(\frac{1 - f_{shad}}{1 - f_{self}}\right)\left[\frac{\sin\theta + 2^{-1/2}\sigma f_{self}\cos\theta}{(1 + 2\sigma^2)^{1/2}}\right] \qquad (17)$$

and

$$\bar{l^2} = \left(\frac{1 - f_{shad}}{1 - f_{self}}\right)\left[\frac{(1 + 0.2\sigma^3)\sin^2\theta + \sigma^2(1 - f_{self})\cos^2\theta}{1 + 2\sigma^2}\right]. \qquad (18)$$

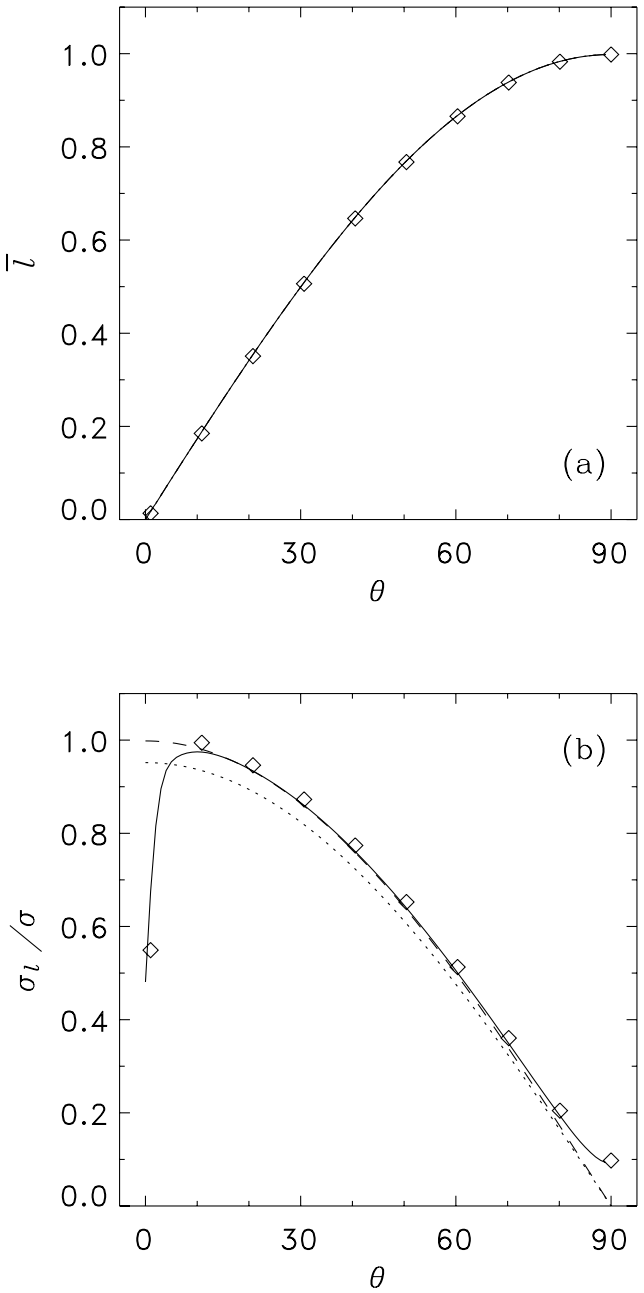

Figure 5. (a) Averages and (b) scaled standard deviations of direct-beam illumination fraction against solar elevation for Trail Valley Creek. Markers are from simulations, dotted lines are from equations (11) and (12), dashed lines are from equations (13) and (14), and solid lines are from equations (17) and (18).

[13] The average $\bar{l}$ and the normalized standard deviation σ_l/σ from simulations and parametrizations are shown for the extreme cases of Trail Valley Creek and Maroon Creek in Figures 5 and 6, respectively. Although the maximum solar elevation is 44 for Trail Valley Creek and 74 for Maroon Creek, the results are shown for the full range of solar elevations up to 90 for generality. Equations (11), (13), and (17) all give good estimates of $\bar{l}$; indeed, for the gentle topography of Trail Valley Creek in Figures 5a, the three lines are indistinguishable. For σ_l, the standard deviation calculated using equations (17) and (18) follows the simulations well at all solar elevations. Results from equations (12) and (14) do not follow each other exactly because the relationship between average slope angle and σ noted above does not hold exactly for the real topographic distributions. Equation (14) generally matches the simulation results better than equation (12) but deviates at low and high solar elevations; these discrepancies may not be significant in practice because incoming radiation is limited by long atmospheric path lengths at low solar elevations, and high solar elevations will not occur at high-latitude sites or during winter [*Dubayah et al.*, 1990].

[14] In addition to direct-beam solar radiation, the surface receives diffuse radiation from the sky and, for nonflat surfaces, radiation reflected from surrounding terrain. Sky

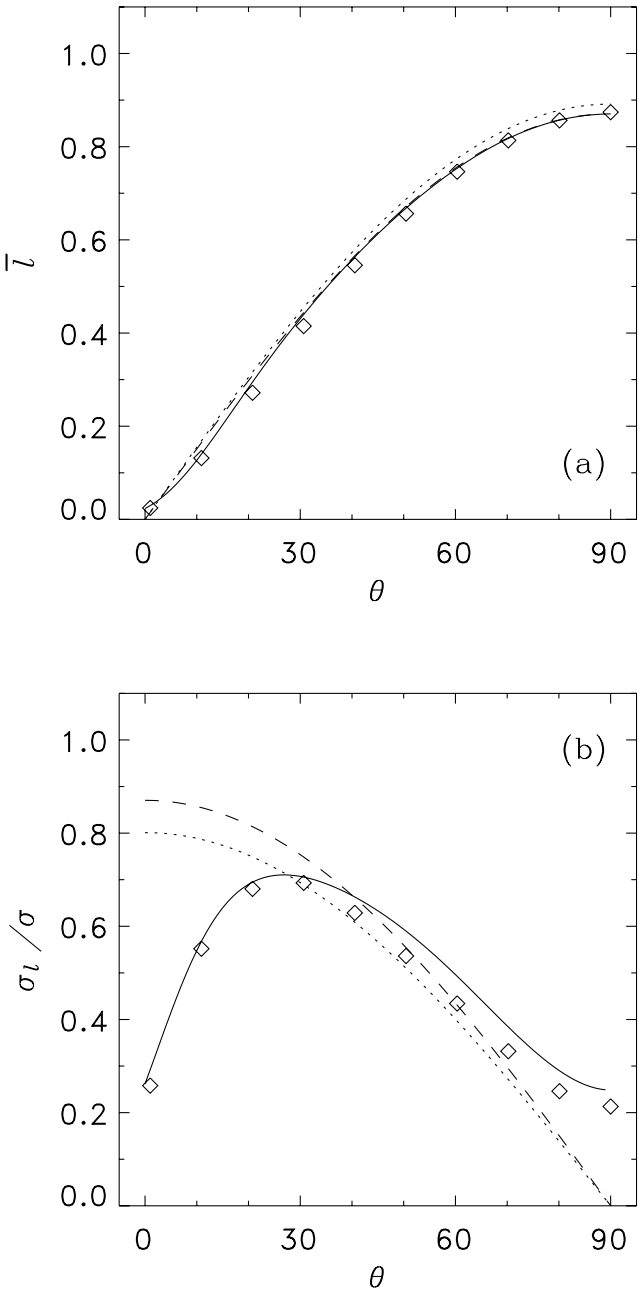

Figure 6. Same as Figure 5, but for Maroon Creek.

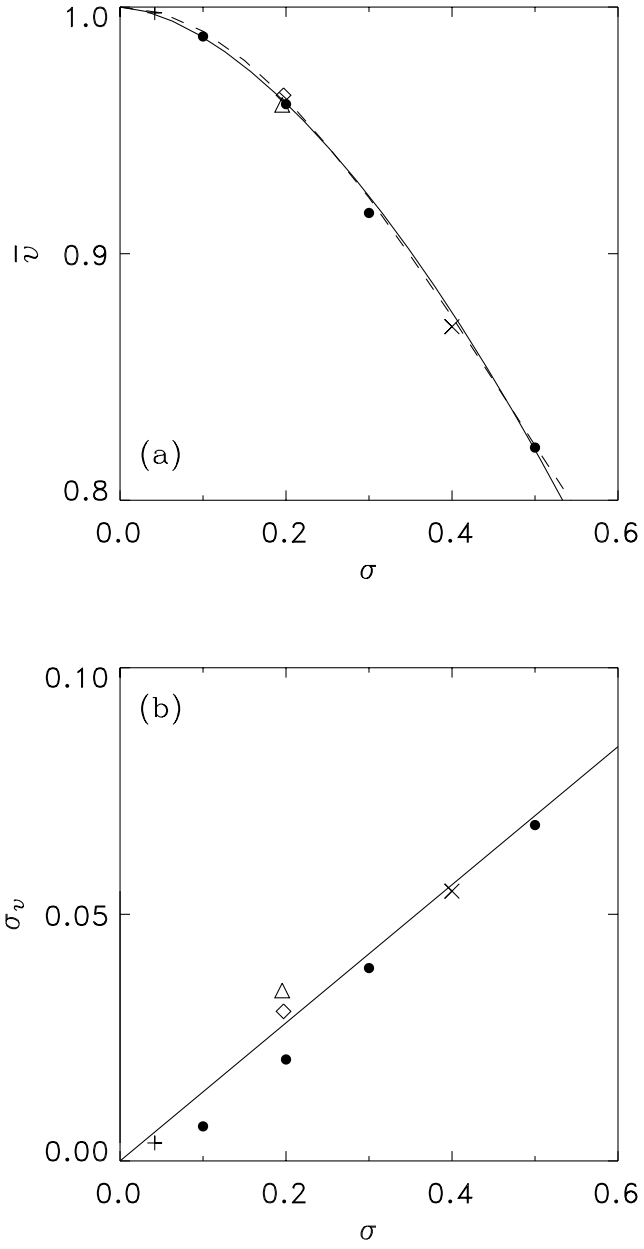

Figure 7. (a) Averages and (b) standard deviations of sky view factors for the four sites (symbols as in Figure 2) and rescaled Maroon Creek topography (circles). Solid lines are a fitted power law in Figure 7a and a linear relationship in Figure 7b, and the dashed line in Figure 7a is given by Monte-Carlo integrations of equation (20).

view has important influences on diffuse solar and thermal radiation at the surface in steep topography. A sky view factor can be calculated for a point by projecting the visible parts of the sky onto the surface, giving

$$v = \frac{1}{2\pi}\int_0^{2\pi} \mathrm{d}\phi \frac{2\cos^2\eta - s_\parallel(\pi - 2\eta - \sin 2\eta)}{2\left(1 + s_\perp^2 + s_\parallel^2\right)^{1/2}}. \quad (19)$$

Integrating over distributions of η, $s_\perp$, and $s_\parallel$ for isotropic topography, noting that the horizon angle in any direction is greater than or equal to $\tan^{-1} s_\parallel$ and changing the order of integration, gives the average sky view as

$$\overline{v} = \int_{-\infty}^{\infty} \frac{p(s_\perp, s_\parallel)\mathrm{d}s_\perp \mathrm{d}s_\parallel}{\left(1 + s_\perp^2 + s_\parallel^2\right)^{1/2}} \int_{\tan^{-1} s_\parallel}^{\pi/2} \mathrm{d}\eta\, p(\eta) \times \left[\cos^2\eta - s_\parallel\left(\frac{\pi}{2} - \eta - \frac{1}{2}\sin 2\eta\right)\right]. \quad (20)$$

Equation (20) can again be evaluated by a Monte-Carlo integration, this time generating three random series for $s_\parallel$, $s_\perp$, and η, and rejecting samples for which $s_\parallel > \tan\eta$. Calculated values are shown in Figure 7a and compared with the results from simulations. A power law $\overline{v} = 1 - 0.57\sigma^{5/3}$ gives a good fit to the results. Standard deviations of v, shown in Figure 7b, have more scatter, but a linear relationship $\sigma_v = 0.14\sigma$ fits quite well. To extend the range of the simulations, sky view was also calculated after rescaling the elevation range of the Maroon Creek DEM by varying amounts; the results from these simulations are shown by circles in Figure 7 and also fall close to the fitted lines.

[15] Solar radiation at the surface depends on topography, latitude, season, time of day, cloud cover, and turbidity of the clear air. Climate models include sophisticated atmospheric radiation schemes [e.g., *Edwards and Slingo*, 1996], and a range of models are available for stand-alone applications [e.g., *Dozier*, 1980]. Here diurnal variations in clear-sky direct-beam and diffuse solar radiation, S_{dir} and S_{dif}, respectively, on a level surface are simulated at 30-minute intervals for each site using the Image Processing Workbench (cirque.nwrc.ars.usda.gov/~ipw). Local surface fluxes of solar radiation over topography are then calculated from

$$S = lS_0 + vS_{\mathrm{dif}}, \quad (21)$$

where $S_0 = S_{\mathrm{dir}}/\sin\theta$. A first approximation for terrain reflections can be included with the modification

$$S = \frac{lS_0 + vS_{\mathrm{dif}}}{1 - (1 - v)\alpha} \quad (22)$$

and a seasonal estimation of surface albedo α; reflected radiation can be important for high albedo snow surfaces, but this is neglected here. From equation (21), the spatial average of solar radiation is

$$\overline{S} = \overline{l}S_0 + \overline{v}S_{\mathrm{dif}}, \quad (23)$$

and the variance is

$$\sigma_S^2 = \sigma_l^2 S_0^2 + \sigma_v^2 S_{\mathrm{dif}}^2 + 2\mathrm{cov}(l, v)S_0 S_{\mathrm{dif}}, \quad (24)$$

where σ_l^2 and σ_v^2 are the variances of l and v, respectively, and cov(l, v) is their covariance. Some covariance can be expected, as locations with restricted sky view are also likely to receive little direct illumination, but the contribution from the covariance term turns out to be small in simulations of σ_S.

[16] Figures 8 and 9 show spatial averages and standard deviations in simulated clear-sky solar radiation for 15 January and 15 June, respectively, at each of the sites. The peak radiation for Reynolds Creek in fact exceeds that

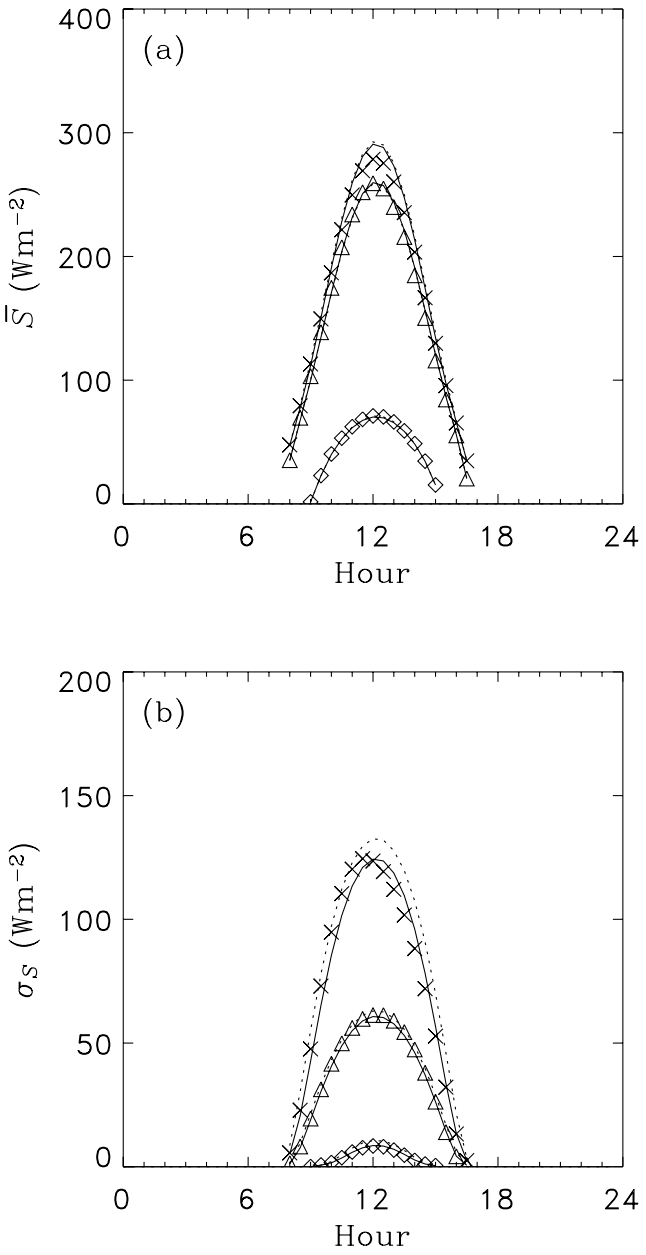

Figure 8. (a) Averages and (b) standard deviations of simulated clear-sky solar radiation on 15 January for the four sites (symbols as in Figure 2). Dotted lines are from equations (13) and (14), and solid lines are from equations (17) and (18).

for Maroon Creek in June despite the former's more northerly location. The standard deviation of solar radiation is limited at low solar elevations by the low incoming radiation and at high solar elevations by the reduction in shading, giving a maximum at an intermediate elevation that depends on optical depth [*Dubayah et al.*, 1990; *Oliphant et al.*, 2003]; this accounts for the "M" shape seen for Reynolds Creek and Maroon Creek in Figure 9b. Despite the anisotropy of the topography, statistics from the simulations are nearly symmetrical about solar noon even for Maroon Creek.

[17] Simulation results in the figures are compared with the modified form of the parametrization of *Dubayah et al.* [1990] given by equations (13) and (14) and the new parametrization given by equations (17) and (18) in Figures 8 and 9. Both parametrizations give extremely good estimates of averages and fairly good estimates of standard deviations of solar radiation. Root mean square errors in averages and standard deviations for the original and modified forms of the parametrization of *Dubayah et al.* [1990] and the new parametrization are given in Tables 1 and 2 for each site and each month of the year. The new parametrization generally gives the best results, especially for standard deviations, but the modified parametrization often gives very similar or even slightly better results.

[18] Results presented here are for clear-sky conditions. The effect of partial cloud cover can easily be incorporated in the parametrization if orographic effects do not lead to clouds forming in strongly preferential locations; for random overlap of topographic shadows and cloud shadows covering

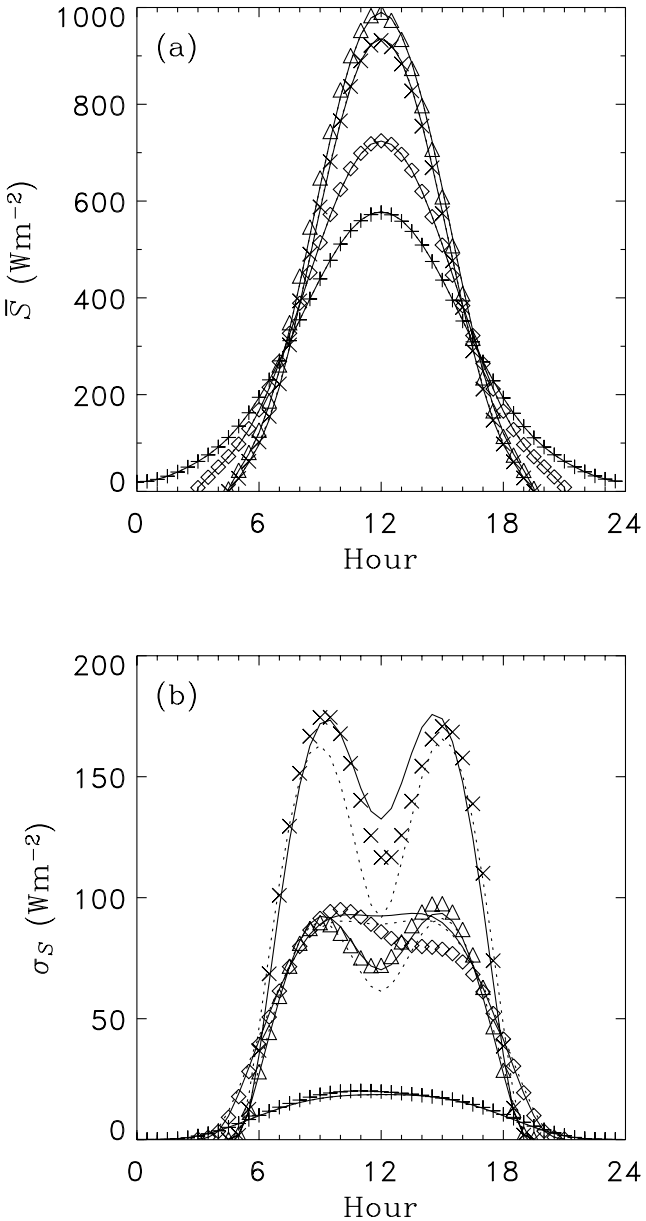

Figure 9. Same as Figure 8, but for 15 June.

Table 1. Root Mean Square Errors for Estimates of the Average Solar Radiation at Each Site and for the 15th Day of Each Month From Equations (11), (13), and (15)

	Site											
	TVC			WC			RC			MC		
	Equation											
Month	(11)	(13)	(15)	(11)	(13)	(15)	(11)	(13)	(15)	(11)	(13)	(15)
Jan	0.00	0.00	0.00	0.06	0.07	0.30	2.23	2.08	2.14	7.75	3.94	4.78
Feb	0.05	0.05	0.05	0.56	0.26	0.40	3.77	3.61	3.61	9.47	3.05	5.57
Mar	0.32	0.30	0.30	1.40	0.35	0.49	5.99	5.71	5.69	10.7	2.24	4.89
Apr	0.69	0.61	0.62	2.55	0.66	0.72	8.39	7.89	7.86	11.5	5.24	3.88
May	0.93	0.80	0.80	3.53	1.13	1.01	9.84	9.12	9.09	11.3	8.45	3.30
Jun	1.02	0.86	0.86	3.97	1.40	1.19	10.4	9.53	9.49	10.9	10.0	3.26
Jul	0.98	0.83	0.83	3.78	1.29	1.12	10.1	9.34	9.30	11.0	9.37	3.24
Aug	0.80	0.70	0.70	2.99	0.86	0.84	9.01	8.43	8.39	11.4	6.75	3.48
Sep	0.48	0.43	0.43	1.84	0.43	0.56	6.97	6.63	6.60	11.0	3.35	4.28
Oct	0.14	0.13	0.13	0.87	0.29	0.36	4.57	4.40	4.38	9.78	2.16	5.19
Nov	0.00	0.00	0.00	0.18	0.10	0.34	2.66	2.52	2.55	8.21	3.53	5.07
Dec	0.00	0.00	0.00	0.06	0.07	0.18	1.90	1.74	1.81	7.15	3.95	4.34

fraction f_{cloud}, adjusted values are given by multiplying equations (17) and (18) by $(1 - f_{\mathrm{cloud}})$.

[19] A statistical-dynamical surface energy balance model incorporating subgrid variations in solar radiation, analogous to the model of *Avissar* [1992], would require probability distributions of radiation. Distributions of direct-beam illumination and slope components are related through

$$p(l) = p(s)\frac{ds}{dl} \tag{25}$$

for $l > 0$, and $p(l = 0) = f_{\mathrm{self}}$. Expanding equation (5) to first order gives $l = \sin\theta + s_{\|}\cos\theta$; putting this in equation (25) and scaling to allow for the fraction of the surface that is in shadow but not self-shaded gives

$$p(l) = \left(\frac{1 - f_{\mathrm{shad}}}{1 - f_{\mathrm{self}}}\right)\frac{1}{\sqrt{2}\sigma\cos\theta}\exp\left(-\frac{\sqrt{2}|l - \sin\theta|}{\sigma\cos\theta}\right). \tag{26}$$

Equation (26) matches simulated illumination distributions well for Trail Valley Creek, Wolf Creek, and Reynolds Creek but gives distributions that are a little too sharply peaked for the steeper topography of Maroon Creek; comparisons are shown for Wolf Creek in Figure 10a and for Maroon Creek in Figure 10b. Distributions of sky view factors, shown in Figure 11 for Reynolds Creek and Maroon Creek, are negatively skewed and bounded above by 1; gamma distributions for $1 - v$ give good fits.

Table 2. Root Mean Square Errors for Estimates of the Standard Deviation in Solar Radiation at Each Site and for 15th Day of Each Month From Equations (12), (14), and (16)

	Site											
	TVC			WC			RC			MC		
	Equation											
Month	(12)	(14)	(16)	(12)	(14)	(16)	(12)	(14)	(16)	(12)	(14)	(16)
Jan	0.00	0.00	0.00	0.15	0.84	0.08	3.17	1.56	0.52	4.18	11.4	3.40
Feb	0.19	0.03	0.03	1.52	2.06	0.72	4.99	1.72	0.64	5.98	12.4	5.56
Mar	1.29	0.23	0.23	4.55	3.40	2.24	7.09	1.45	1.09	8.43	12.4	8.35
Apr	2.77	0.49	0.49	7.58	4.95	4.11	9.17	1.35	1.49	11.1	10.1	9.63
May	3.75	0.66	0.65	9.60	5.23	4.75	10.5	2.56	1.91	13.8	7.58	8.43
Jun	4.14	0.72	0.71	10.5	5.09	4.77	11.1	3.50	2.19	15.6	8.11	7.54
Jul	3.97	0.70	0.68	10.1	5.13	4.75	10.9	3.09	2.07	14.8	7.64	7.84
Aug	3.22	0.57	0.57	8.49	5.08	4.45	9.72	1.77	1.63	12.1	8.43	9.07
Sep	1.92	0.34	0.34	5.88	4.08	3.10	7.92	1.22	1.25	9.50	11.3	9.13
Oct	0.57	0.10	0.10	2.79	2.42	1.25	5.77	1.58	0.81	6.95	12.2	6.73
Nov	0.01	0.01	0.01	0.35	1.16	0.23	3.76	1.51	0.51	4.55	11.2	4.06
Dec	0.00	0.00	0.00	0.13	0.46	0.03	2.67	1.52	0.48	4.04	11.2	2.92

4. Scaling

[20] *Dubayah et al.* [1990], *Mckenney et al.* [1999], and *Pohl et al.* [2006] have discussed the influence of DEM

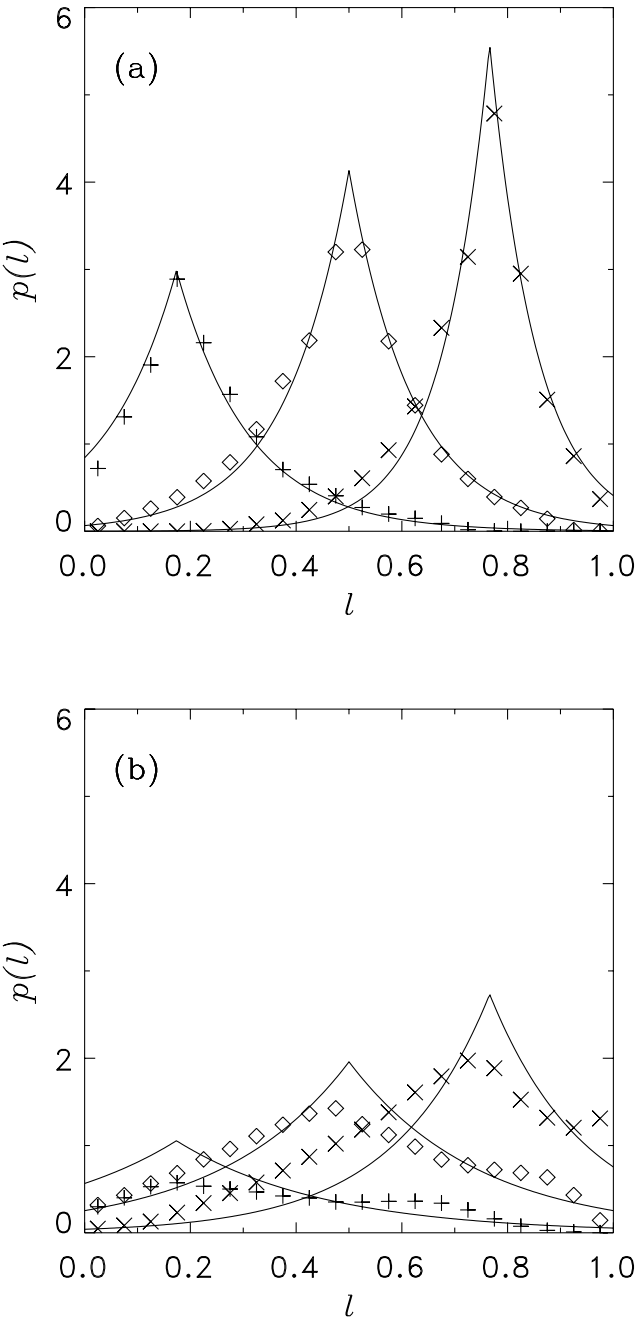

Figure 10. Distributions of direct-beam illumination fraction from simulations with solar elevations of 10 (+), 30 (◇), and 50 (×) for (a) Wolf Creek and (b) Maroon Creek. The lines are from equation (26).

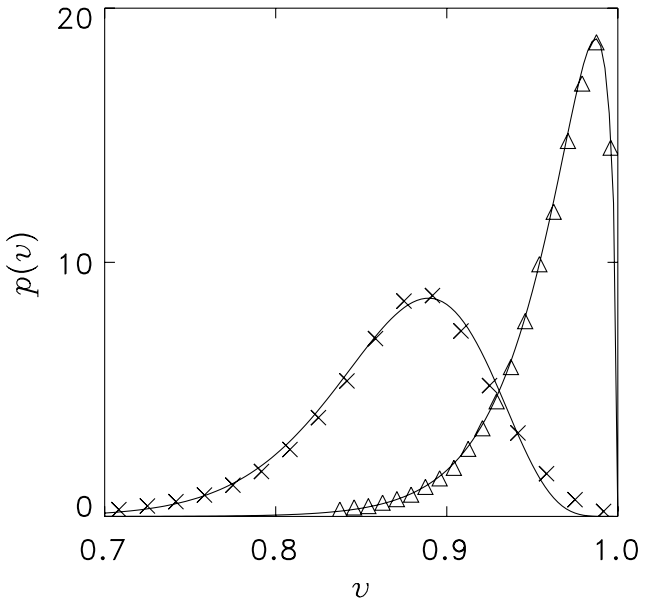

Figure 11. Simulated distributions of sky view factors for Reynolds Creek (△) and Maroon Creek (×). The lines are gamma distributions of $1 - v$.

resolution on statistics of simulated radiation distributions over moderate topography. The standard deviation of slope components emerged above as the parameter controlling averages and standard deviations of solar radiation over topographic surfaces. Because calculated slopes will decrease as the resolution of the DEM decreases, consideration has to be given to how σ scales with resolution. For the Trail Valley Creek topography, *Essery* [2001] found that slope components have an approximately exponential autocorrelation. Sampling topography with exponentially autocorrelated slopes and correlation length ξ at resolution Δx gives the standard deviation

$$\sigma(\Delta x) = \sigma_0 \left\{ \frac{2\xi}{\Delta x} \left[1 + \frac{\xi}{\Delta x} \left(e^{-\Delta x/\xi} - 1 \right) \right] \right\}^{1/2}, \qquad (27)$$

where σ_0 is the value approached asymptotically for vanishing Δx. Standard deviations calculated by resampling DEMs at progressively coarser resolutions are shown and compared with equation (27) in Figure 12. Correlation lengths obtained by least squares fits to equation (27) are 65, 100, 62, and 91 m for Trail Valley Creek, Wolf Creek, Reynolds Creek and Maroon Creek, respectively. Scaling Δx by these correlation lengths collapses the results onto a single curve.

[21] Horizon angles and sky view are much more expensive to compute than slope components. It was shown above that the average sky view factor scales as a power of σ, giving a more convenient parametrization. Under a rescaling $z \to \lambda z$ for a particular topography, $\sigma \to \lambda\sigma$ and $\eta \to \tan^{-1}(\lambda \tan\eta) \approx \lambda\eta$ for every horizon angle, suggesting a linear scaling of horizon angle statistics with σ. In fact, it is found that linear fits $\overline{\eta} = 35.7\sigma$ and $\sigma_\eta = 32.7\sigma$ give errors of less than 2 and r^2 exceeding 0.97 in comparison with horizon angle calculations for the four sites.

[22] Although calculations of slope statistics are expensive for applications in models with large grid cells or a large number of cells, these calculations are straightforward and need only to be performed once [*Müller and Scherer*, 2005]. Alternatively, standard deviations of slope components might be parametrized as a function of standard deviations of elevation on the assumption that both measures will have larger values for more mountainous topography; standard deviation of elevation is already commonly used as an input to atmospheric models for parametrizations of orographic drag [*Milton and Wilson*, 1996]. Figure 13 shows standard deviations of slope components against standard deviations of elevation for the four sites considered here and for 132 separate 12 × 12 km areas covering the Colorado Rockies. Standard deviations of slope and elevation have correlations of 0.97 for the four sites and 0.64 for the Colorado DEM samples; the best fit is given by $\sigma = \Lambda^{-1}\sigma_z$ with $\Lambda \approx 900$ m in both cases.

[23] In addition to variations in radiation, coupled surface energy and mass balances are also influenced by variations in air temperature, wind speed, and precipitation with elevation. Slope and elevation vary on a range of length scales in regions of complex topography. Variability length scales can be investigated by calculating average standard deviations for samples of area L^2 within a DEM and by varying the sample length scale L. Figure 14a plots standard deviations of southerly slope components scaled by values for the entire DEMs against L scaled by the correlation lengths determined above. The results for the four sites again fall close to a single curve and show that 50% of the standard deviation in slope components is accounted for by variations on scales shorter than 2ξ. There is more scatter between sites in standard deviation of elevation (Figure 14b), but less than 10% of the standard deviation is captured by sampling on length scale 2ξ in all cases. This is not a surprising result; slope components are partial derivatives of elevation, and the differentiation can be regarded as a filter

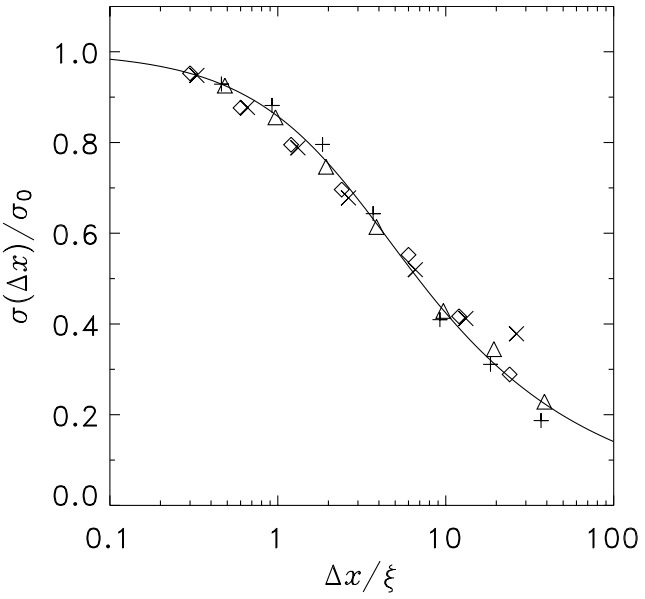

Figure 12. Standard deviations of slope components against DEM resolution Δx scaled by correlation length ξ (symbols as in Figure 2). The line is given by equation (27).

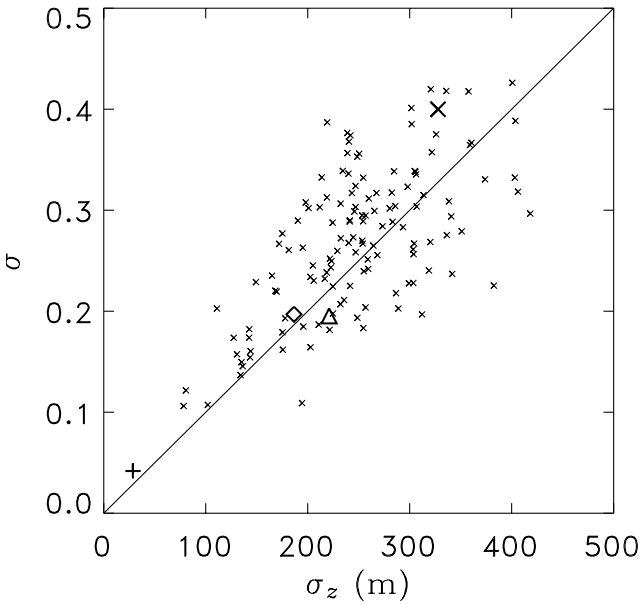

Figure 13. Standard deviations of slope components against standard deviations of elevation for the four sites (symbols as in Figure 2) and for 132 separate 12 × 12 km areas covering the Colorado Rockies (small crosses).

amplifying short-wavelength fluctuations in Fourier space. The scale separation suggests that elevation band models intended to represent large-scale influences of elevation could be modified to include small-scale radiative influences of slope and aspect.

5. Conclusions

[24] Statistical descriptions of topography and simulated clear-sky solar radiation were considered for the four areas in North America. It was found that slope components and horizon angles could be described by Laplace and extreme value distributions, respectively. From these distributions, parametrizations were developed for the fraction of the surface in shadow and for spatial averages, standard deviations, and distributions of direct-beam and diffuse solar radiation. These parametrizations depend on the solar elevation and the standard deviation of slope components along the solar azimuth, which can be characterized by a single parameter for isotropic topography or three parameters (variances of westerly and southerly slope components and their covariance) for anisotropic topography. Inputs of direct-beam and diffuse solar radiation are also required and were provided by a two-stream atmospheric radiation model. Results from the parametrizations compared well with statistics from explicit simulations of solar radiation over the four areas. Good results were also obtained using a modified version of the simpler parametrizations of *Dubayah et al.* [1990], even over much more extreme topography than that for which they were developed.

[25] Standard deviations of slope components were found to scale with the resolution of the DEM in the same way for each of the sites and have a linear relationship with standard deviations of elevation. Correlation lengths are much shorter for slope components than for elevations, so it may be possible to separate the influences of slope and aspect on the surface energy balance from influences of elevation in parametrizations for areas of high relief. This investigation has been restricted to mesoscale areas; global climate models operate on much larger grid scales for which there will be a greater chance of nonstationarity in subgrid statistics. More work is required on topographic statistics at large scales, but a division into elevation bands might again provide a suitable stratification for parametrizations.

[26] Energy is conserved but radiation density is decreased over complex topography because the surface area contained within grid cells is increased relative to a flat surface. This directly impacts the surface energy balance, but subgrid variability will only influence the average energy balance through nonlinearities. In future work, we

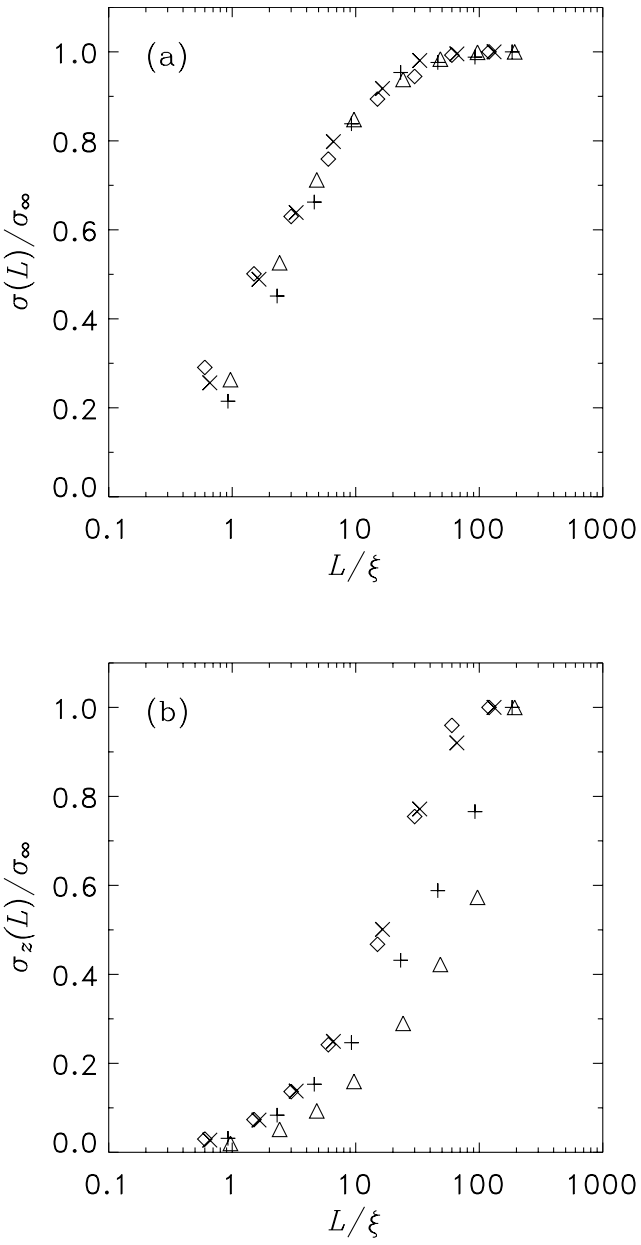

Figure 14. Scaled standard deviations of (a) slope components and (b) elevations plotted against scaled sample length (symbols as in Figure 2).

intend to investigate this for simulations of snowmelt in mountainous regions.

[27] **Acknowledgments.** Digital elevation data were supplied by the National Water Research Institute, Saskatoon (Trail Valley Creek and Wolf Creek), the US Department of Agriculture Northwest Watershed Research Center (Reynolds Creek), and the US Geological Survey (Maroon Creek). This work was supported in part by NOAA GEWEX Americas Prediction Program (GAPP) Project 5362-13610-006-06R (NOAA). R.E. is supported by NERC Advanced Research Fellowship NER/J/S/2001/00812 and acknowledges the research support and hospitality of the USDA Agricultural Research Service Northwest Watershed Research Center while conducting parts of this work. We thank Ralph Dubayah and two anonymous referees for their comments on this paper.

References

Agassi, E., and N. Ben Yosef (1997), Influence of scene topography on the observed correlation between thermal infrared and visible/near-infrared images of ground terrain, *Int. J. Remote Sens.*, *18*, 3853–3865.

Arola, A., and D. P. Lettenmaier (1996), Effects of subgrid spatial heterogeneity on GCM-scale land surface energy and moisture fluxes, *J. Clim.*, *9*, 1339–1348.

Arrell, K. E., and I. S. Evans (2003), Predicting glacier distributions: local climate predictions, paper presented at the 60th Eastern Snow Conference, Sherbrooke, Quebec.

Avissar, R. (1992), Conceptual aspects of a statistical-dynamical approach to represent landscape subgrid-scale heterogeneities in atmospheric models, *J. Geophys. Res.*, *97*, 2729–2742.

Avissar, R., and R. Pielke (1989), A parametrization of heterogeneous land surfaces for atmospheric numerical models and its impact on regional meteorology, *Mon. Weather Rev.*, *117*, 2113–2136.

Baral, D. J., and R. P. Gupta (1997), Integration of satellite sensor data with DEM for the study of snow cover distribution and depletion pattern, *Int. J. Remote Sens.*, *18*, 3889–3894.

Blöschl, G., R. Kirnbauer, and D. Gutknecht (1991), Distributed snowmelt simulations in an alpine catchment: 1. Model evaluation on the basis of snow cover patterns, *Water Resour. Res.*, *27*, 3171–3179.

Bowling, L. C., J. W. Pomeroy, and D. P. Lettenmaier (2004), Parameterisation of the sublimation of blowing snow in a macroscale hydrology model, *J. Hydrometeorol.*, *5*, 745–762.

Cline, D., R. E. Davis, W. Edelstein, J. Hilland, K. McDonald, S. Running, J. Way, and J. van Zyl (1999), Cold Land Processes Mission (EX-7): Science and technology implementation plan, Report on the NASA Post-2002 Land Surface Hydrology Planning Workshop Irvine, CA, 12–14 April 1999. Available online from http://www.nohrsc.nws.gov/~cline/clp.html.

Corripio, J. G. (2003), Vectorial algebra algorithms for calculating terrain parameters from DEMs and solar radiation modelling in mountainous terrain, *Int. J. Geogr. Inf. Sci.*, *17*, 1–23.

Cox, P. M., R. A. Betts, C. D. Jones, S. A. Spall, and I. J. Totterdell (2000), Acceleration of global warming due to carbon-cycle feedbacks in a coupled climate model, *Nature*, *408*, 184–187.

Dozier, J. (1980), A clear-sky spectral solar radiation model for snow-covered mountainous terrain, *Water Resour. Res.*, *16*, 709–718.

Dozier, J., and J. Frew (1990), Rapid calculation of terrain parameters for radiation modelling from digital elevation data, *IEEE Trans. Geosci. Remote Sens.*, *28*, 963–969.

Dubayah, R., J. Dozier, and F. W. Davis (1990), Topographic distribution of clear-sky radiation over the Konza Prairie, Kansas, *Water Resour. Res.*, *26*, 679–690.

Dubayah, R., and P. Rich (1995), Topographic solar radiation models for GIS, *Int. J. Geogr. Inf. Sci.*, *9*, 405–419.

Durand, Y., G. Giraud, E. Brun, L. Merindol, and E. Martin (1999), A computer-based system simulating snowpack structures as a tool for regional avalanche forecasting, *J. Glaciol.*, *45*, 469–484.

Edwards, J., and A. Slingo (1996), Studies with a flexible new radiation code: 1. Choosing a configuration for a large-scale model, *Q. J. R. Meteorol. Soc.*, *122*, 689–720.

Essery, R. L. H. (2001), Spatial statistics of windflow and blowing snow fluxes over complex topography, *Bound. Layer Meteorol.*, *100*, 131–147.

Essery, R. L. H. (2003), Aggregated and distributed modelling of snow cover for a high-latitude basin, *Glob. Planet. Change*, *38*, 161–164.

Essery, R. L. H., M. J. Best, R. A. Betts, P. M. Cox, and C. M. Taylor (2003), Explicit representation of subgrid heterogeneity in a GCM land-surface scheme, *J. Hydrometeorol.*, *4*, 530–543.

Essery, R. L. H. (2004), Statistical representation of mountain shading, *Hydrol. Earth Syst. Sci.*, *8*, 1045–1050.

Franklin, J. (1998), Predicting the distribution of shrub species in southern California from climate and terrain-derived variables, *J. Veg. Sci.*, *9*, 733–748.

Fu, P., and P. M. Rich (2002), A geometric solar radiation model with applications in agriculture and forestry, *Comput. Electron. Agric.*, *37*, 25–35.

Garnier, B. J., and A. Ohmura (1968), A method of calculating the direct shortwave radiation income of slopes, *J. Appl. Meteorol.*, *7*, 796–800.

Gumbel, E. J. (1958), Statistics of extremes, 375 pp., Columbia Univ. Press, New York.

Hauge, G., and L. R. Hole (2003), Implementation of slope irradiance in Mesoscale Model version 5 and its effect on temperature and wind fields during the breakup of a temperature inversion, *J. Geophys. Res.*, *108*(D2), 4058, doi:10.1029/2002JD002575.

Kirnbauer, R., G. Blöschl, and D. Gutknecht (1994), Entering the era of distributed snow models, *Nord. Hydrol.*, *25*, 1–24.

Koenderink, J. J., A. J. van Doorn, K. J. Dana, and S. Nayar (1999), Bidirectional reflection distribution function of thoroughly pitted surfaces, *Int. J. Comput. Vis.*, *31*, 129–144.

Kondratyev, K. Ya., and M. P. Manolova (1960), The energy balance of slopes, *Sol. Energy*, *4*, 14–19.

Koster, R. D., and M. J. Suarez (1992), Modelling the land surface boundary in climate models as a composite of independent vegetation stands, *J. Geophys. Res.*, *97*, 2697–2715.

Kumar, L., A. K. Skidmore, and E. K. Nowles (1997), Modelling topographic variation in solar radiation in a GIS environment, *Int. J. Geogr. Inf. Sci.*, *11*, 475–497.

Lundquist, J. D., and A. L. Flint (2006), Onset of snowmelt and streamflow in 2004 in the Western United States: How shading may affect spring streamflow timing in a warmer world, *J. Hydrometeorol.*, *7*, 1199–1217.

Margot, J. L., D. B. Campbell, R. F. Jurgens, and M. A. Slade (1999), Topography of the lunar poles from radar interferometry: A survey of cold trap locations, *Science*, *284*, 1658–1660.

Marks, D., J. Domingo, D. Susong, T. Link, and D. Garen (1999), A spatially distributed energy balance snowmelt model for application in mountain basins, *Hydrol. Process.*, *13*, 1935–1959.

Mckenney, D. W., B. G. Mackey, and B. L. Zavitz (1999), Calibration and sensitivity analysis of a spatially-distributed solar radiation model, *Int. J. Geogr. Inf. Sci.*, *13*, 49–65.

Milton, S. F., and C. A. Wilson (1996), The impact of parameterized subgrid-scale orographic forcing on systematic errors in a global NWP model, *Mon. Weather Rev.*, *124*, 2023–2045.

Müller, M. D., and D. Scherer (2005), A grid- and subgrid-scale radiation parameterization of topographic effects for mesoscale weather forecast models, *Mon. Weather Rev.*, *133*, 1431–1442.

Oliphant, A. J., R. A. Spronken-Smith, A. P. Sturman, and I. F. Owens (2003), Spatial variability of surface radiation fluxes in mountainous terrain, *J. Appl. Meteorol.*, *42*, 113–128.

Pohl, S., P. Marsh, and A. Pietroniro (2006), Spatial-temporal variability in solar radiation during spring snowmelt, *Nord. Hydrol.*, *37*, 1–19.

Reuter, H. I., K. C. Kersebaum, and O. Wendroth (2005), Modelling of solar radiation influenced by topographic shading—evaluation and application for precision farming, *Phys. Chem. Earth*, *30*, 143–149.

Rouse, W. R. (1999), Progress in hydrological research in the Mackenzie GEWEX study, *Hydrol. Process.*, *14*, 1667–1685.

Shuttleworth, W. J. (1988), Macrohydrology: The new challenge for process hydrology, *J. Hydrol.*, *100*, 31–56.

Slaughter, C. W., D. Marks, G. N. Flerchinger, S. S. van Vactor, and M. Burgess (2001), Thirty-five years of research data collection at Reynolds Creek Experimental Watershed, Idaho, United States, *Water Resour. Res.*, *37*, 2819–2823.

Sloan, W. T., C. G. Kilsby, and R. Lunn (2004), Incorporating topographic variability into a simple regional snowmelt model, *Hydrol. Process.*, *18*, 3371–3390.

Strasser, U., J. Corripio, F. Pellicciotti, P. Burlando, B. Brock, and M. Funk (2004), Spatial and temporal variability of meteorological variables at Haut Glacier d'Arolla (Switzerland) during the ablation season 2001: Measurements and simulations, *J. Geophys. Res.*, *109*, D03103, doi:10.1029/2003JD003973.

Walland, D. J., and I. Simmonds (1996), Sub-grid-scale topography and the simulation of Northern Hemisphere snow cover, *Int. J. Climatol.*, *16*, 961–982.

Wood, E. F., D. P. Lettenmaier, and V. G. Zartarian (1992), A land-surface hydrology parameterization with subgrid variability for general circulation models, *J. Geophys. Res.*, *97*, 2717–2728.

R. Essery, Centre for Glaciology, Institute of Geography and Earth Sciences, University of Wales Aberystwyth, Aberystwyth SY23 3DB, UK. (rie@aber.ac.uk)

D. Marks, USDA Agricultural Research Service, Northwest Watershed Research Center, Boise, ID 83712, USA.